Highly time-resolved chemical characterization and implications of regional transport for submicron aerosols in the North China Plain

Li, Jiayun

2020-02-25

Li , J , Liu , Z , Cao , L , Gao , W , Yan , Y , Mao , J , Zhang , X , He , L , Xin , J , Tang , G , Ji , D , Hu , B , Wang , L , Wang , Y , Dai , L , Zhao , D , Du , W & Wang , Y 2020 , ' Highly time-resolved chemical characterization and implications of regional transport for submicron aerosols in the North China Plain ' , The Science of the Total Environment , vol. 705 , 135803 . https://doi.org/10.1016/j.scitotenv.2019.135803

http://hdl.handle.net/10138/351099
https://doi.org/10.1016/j.scitotenv.2019.135803

Science of the Total Environment xxx (xxxx) xxx

Contents lists available at ScienceDirect

Science of the Total Environment

journal homepage: www.elsevier.com/locate/scitotenv

Highly time-resolved chemical characterization and implications of regional transport for submicron aerosols in the North China Plain

Jiayun Li [a,c], Zirui Liu [a,*], Liming Cao [d], Wenkang Gao [a], Yingchao Yan [a,c], Jia Mao [f], Xinghua Zhang [e], Lingyan He [d], Jinyuan Xin [a,b,c], Guiqian Tang [a], Dongsheng Ji [a], Bo Hu [a], Lili Wang [a], Yonghong Wang [i], Lindong Dai [a], Dandan Zhao [a,c], Wupeng Du [h], Yuesi Wang [a,b,**]

[a] State Key Laboratory of Atmospheric Boundary Layer Physics and Atmospheric Chemistry (LAPC), Institute of Atmospheric Physics, Chinese Academy of Sciences, Beijing 100029, China
[b] Center for Excellence in Regional Atmospheric Environment, Institute of Urban Environment, Chinese Academy of Sciences, Xiamen 361021, China
[c] University of Chinese Academy of Sciences, Beijing 100049, China
[d] Key Laboratory for Urban Habitat Environmental Science and Technology, Peking University Shenzhen Graduate School, Shenzhen 518055, China
[e] Key Laboratory of Arid Climatic Change and Reducing Disaster of Gansu Province, Key Laboratory of Arid Climatic Change and Disaster Reduction of CMA, Institute of Arid Meteorology, China Meteorological Administration, Lanzhou 730020, China
[f] College of Atmospheric Physics, Nanjing University of Information Engineering, Nanjing 210044, China
[g] Institute for Atmospheric and Earth System Research/Physics, Faculty of Science, University of Helsinki, Finland
[h] Beijing Municipal Climate Center, Beijing 100089, China

HIGHLIGHTS

- First simultaneous observations of PM_1 at urban/background sites in the NCP
- Higher fractions of SOA and SIA in PM_1 were observed in the background area.
- Abundant ammonia emissions in the NCP favor nitrate formation on a regional scale
- Heterogeneous formation of SOA and sulfate is more efficient in the urban area.
- Water vapor transport enhances secondary transformation during regional haze episode.

GRAPHICAL ABSTRACT

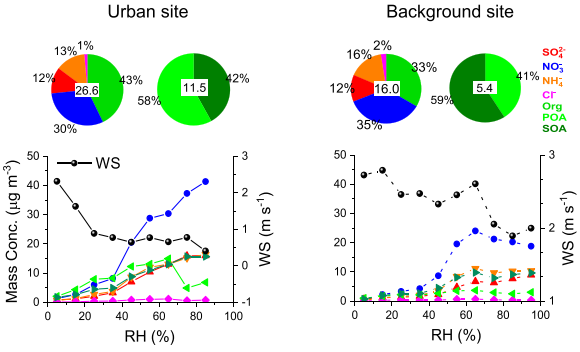

ARTICLE INFO

Article history:
Received 18 November 2019
Received in revised form 22 November 2019
Accepted 26 November 2019
Available online xxxx

Editor: Jianmin Chen

Keywords:
Submicron aerosols
Chemical compositions

ABSTRACT

To investigate the regional transport and formation mechanisms of submicron aerosols in the North China Plan (NCP), for the first time, we conducted simultaneous combined observations of the non-refractory submicron aerosols (NR-PM_1) chemical compositions using aerosol mass spectrometer at urban Beijing (BJ) and at regional background area of the NCP (XL), from November 2018 to January 2019. During the observation period, average mass concentrations of PM_1 in BJ and XL were 26.6 ± 31.7 and 16.0 ± 18.7 μg m^{-3} respectively. The aerosol composition in XL showed a lower contribution of organic aerosol (33% vs. 43%) and higher fractions of nitrate (35% vs. 30%), ammonium (16% vs. 13%), and chlorine (2% vs. 1%) than in BJ. Additionally, a higher contribution of secondary organic aerosol (SOA) was also observed in XL, suggesting low primary emissions and highly oxidized OA in the background area. Nitrate displayed a significantly enhanced contribution with the aggravation of aerosol pollution in both BJ and XL, which was completely neutralized by excess ammonium at both sites, suggesting

* Correspondence to: Z. Liu, Y. Wang, State Key Laboratory of Atmospheric Boundary Layer Physics and Atmospheric Chemistry (LAPC), Institute of Atmospheric Physics, Chinese Academy of Sciences, Beijing 100029, China.
E-mail addresses: liuzirui@mail.iap.ac.cn (Z. Liu), wys@dq.cern.ac.cn (Y. Wang).

https://doi.org/10.1016/j.scitotenv.2019.135803
0048-9697/

Regional transport
NCP

that the abundant ammonia emissions in the NCP favor nitrate formation on a regional scale. In addition, a higher proportion of nitrate in XL can be attributed to the more neutral and higher oxidation capacity of the background atmosphere. Heterogeneous aqueous reaction plays an important role in sulfate and SOA formation, and is more efficient in BJ which can be attributed to the higher aerosol surface areas at urban site. Regional transport from the southwestern regions of NCP showed a significant impact on the formation of haze episodes. Beside the invasion of transported pollutants, the abundant water vapor associated with the air mass to the downwind background area further enhanced local secondary transformation and expanded the regional scope of the haze pollution in the NCP.

1. Introduction

The North China Plan (NCP) has been undergoing rapid urbanization and industrialization, resulting in a dramatic increase in anthropogenic aerosols over the past decade (Che et al., 2009; Huang et al., 2014; Li et al., 2018; Yuan et al., 2015; Zhao et al., 2011; Liu et al., 2015). Numerous anthropogenic aerosols can decrease visibility, affect the climate, and pose a threat to human health (Kanakidou et al., 2005; Shiraiwa et al., 2017; Zhang et al., 2015). For these reasons, various offline and online techniques have been conducted to investigate the characteristics of aerosol particles and the formation mechanisms of haze pollution in the NCP (Hu et al., 2017; Huang et al., 2017; G. Liu et al., 2019; Z. Liu et al., 2019; Ma et al., 2017; Sun et al., 2015a; Wang et al., 2013; W. Xu et al., 2019; Wang et al., 2014). Among these techniques, the aerodyne aerosol mass spectrometer (AMS) is unique because it is capable of getting size-resolved chemical information of non-refractory submicron aerosols (NR-PM_1) (Aiken et al., 2009; DeCarlo et al., 2006). Numerous studies have been performed using AMS, and a variety of views have been proposed (Hu et al., 2017; Hu et al., 2016; Huang et al., 2018; Li et al., 2018; Sun et al., 2014; Sun et al., 2016). The chemical compositions and sources in different cities of the NCP are quite different (Chen et al., 2018; Ge et al., 2017; Hu et al., 2017; Huang et al., 2018; Li et al., 2017; Li et al., 2018). For example, nitrate was the dominant inorganic component in Beijing in recent years (Chen et al., 2018; Ge et al., 2017); however, in industrialized cities southwest of Beijing, sulfate and primary emissions dominated by coal and biomass combustion account for a large proportion of fine particulate matter (Huang et al., 2018; Li et al., 2017). The formation mechanisms of secondary aerosols in the NCP have been widely investigated. For example, Sun et al. (2013a) elucidated the important roles of liquid water in aerosol processing at elevated RH levels, in particular, those affecting sulfate and coal combustion organic aerosol (OA) via aqueous-phase reaction and gas-particle partitioning associated with water uptake, respectively. Duan et al. (2019) found that photochemical oxidation dominated secondary organic aerosol (SOA) formation during late summer, autumn and early winter, and for sulfate formation, gas-phase photochemical oxidation was the major pathway in late summer, and heterogeneous processes were likely more important in autumn and early winter. Xu et al. (2017) further found that aqueous-phase processing has a dominant impact on the formation of more oxidized SOA (MO-OOA), while photochemical processing dominates the formation of less oxidized SOA (LO-OOA). In addition, the impacts of regional transport on the formation and evolution of pollution events were also extensively studied (Sun et al., 2015a; Sun et al., 2015b; Zhao et al., 2017).

The majority of previous studies on haze pollution using the AMS in NCP were single-site measurements and concentrated on urban areas such as Beijing, Handan, and Shijiazhuang. Since haze pollution in the NCP has remarkable regional characteristics, single-site studies cannot fully determine the overall characteristics of the haze pollution in the NCP region. It is also difficult to directly compare these results among single-site studies to conduct a regional assessment. It is suggested that the chemical compositions of particles at the background sites could reflect the characteristics of regional air pollution. Studies in the regional background area in comparison with those in urban areas can provide valuable information on the impacts of anthropogenic activities as well as help to understand air pollution on a regional scale. Despite this, there are few studies on the chemical characteristics of fine particles at background sites, especially studies that are synchronous with urban sites. Z. Liu et al. (2018) found that the contribution of secondary aerosols on polluted days increased at both urban and nearby background sites. Huang et al. (2017) further found that coal combustion, motor vehicle exhaust, secondary inorganic aerosol, dust, and industrial processes were the main sources of $PM_{2.5}$ in urban areas, while secondary aerosol was the dominant source at the background site. Moreover, few studies have emphasized the influence of the long-range transportation of anthropogenic aerosols from southern urban areas to background regions (Pan et al., 2013; Zhu et al., 2014). These results illustrated the significant impacts of regional transport and formation mechanisms of secondary aerosol particles on haze pollution in the NCP. However, these synchronous studies at urban and background sites were based on low-resolution observations, without specifically illuminating the rapid different evolutions and formation mechanisms of regional haze pollution. Due to the limited high-resolution synchronous studies at urban and background sites, our knowledge of the rapid changes in regional transport and formation mechanisms of secondary aerosol particles on different spatial scales is far from complete.

In this work, we present the first simultaneously conducted observations of 5 min time-resolved NR-PM_1 measurements using an HR-ToF-AMS at an urban site (Beijing) and using a Q-AMS at a background site (Xinglong). This study considers a comparison between an urban and a rural site to explore the differences in secondary aerosol formation and regional transport resulting from different emissions and meteorological conditions. Furthermore, we explored rapid changes in regional transport and the formation mechanisms of secondary aerosol particles in BJ and XL based on a detailed analysis of a typical haze episode.

2. Experimental methods

2.1. Sampling sites

The field observations were comprehensively conducted at an urban site (BJ) and a regional background site (XL) located in the northern part of the NCP (Fig. 1), from 10 November 2018 to 31 January 2019. The urban site was located at the Institute of Atmospheric Physics (IAP) of the Chinese Academy of Sciences (39°58′N; 116°22′E; 45 m a.s.l.), which is between the north 3rd and 4th Ring Roads in BJ. This area is a typical urban site that is impacted by local emission sources, such as local traffic and cooking emissions (Liu et al., 2016; Sun et al., 2013b).

The regional background site (XL) is located south of the Yanshan Mountains (north of the Hebei Province) with an elevation of 960 m a.s.l. (40°24′N; 117°40′E; 960 m a.s.l.; Fig. 1), which is approximately 115 km in a straight line from northeast of downtown BJ (Pan et al., 2013). The surroundings of XL site are covered with trees and bushes, and villagers in this arcadia live on fruit trees and are farmers. Because there are no serious local emissions except for a few villages at the foot of the mountain, the XL site is characterized by its background-like nature. Thus, it can be considered an ideal receptor site for regional-scale air pollution in the NCP region (Wang et al., 2013). In

Please cite this article as: J. Li, Z. Liu, L. Cao, et al., Highly time-resolved chemical characterization and implications of regional transport for submicron ..., Science of the Total Environment, https://doi.org/10.1016/j.scitotenv.2019.135803

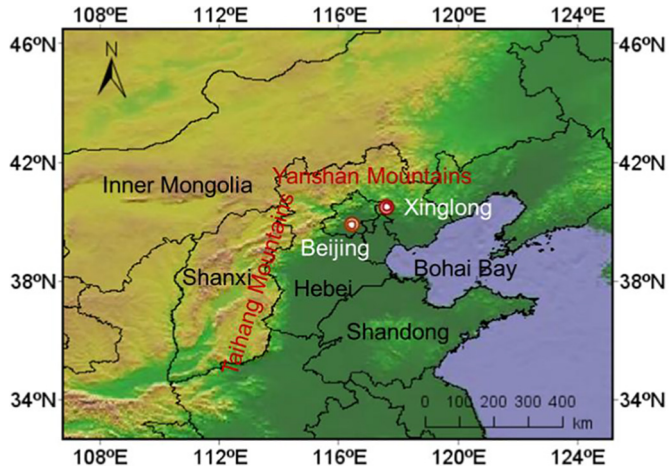

Fig. 1. Map of the observation stations and local topography.

the presence of southwest winds, the XL site is located downwind of the BJ site, and the influence from the urban areas should not be underestimated. Therefore, it is an ideal transport site capable of obtaining a regional signature of pollutants. In addition, XL county was located approximately 10 km northwest of the XL site. The sampler was located on the rooftop of a building (8 m above the ground) at the site.

2.2. Instrumentation and operation

The HR-ToF-AMS and Q-AMS were deployed at the BJ and XL sites, respectively, for the synchronous measurements of NR-PM_1 from 10 November 2018 to 31 January 2019. The HR-ToF-AMS was situated in a sampling room located on the ground floor. The ambient air was drawn into the sampling room through a stainless steel tube with a flow rate of 3 L min^{-1}, of which ~0.085 L min^{-1} was isokinetically sampled into the AMS. A URG cyclone (URG-2000-30ED, URG Inc., North Carolina, USA) was used in front of the sampling inlet to remove coarse particles with size cutoffs of 2.5 μm in terms of aerodynamic diameter. A silica gel diffusion dryer was also set up in front of the inlet system to avoid water vapor condensation, which reduces the uncertainties in particle collection efficiency (CE) due to variable humidity (Middlebrook et al., 2012). Detailed descriptions of the HR-ToF-AMS operation and data treatment are available elsewhere (Aiken et al., 2009; DeCarlo et al., 2006). During this campaign, the HR-ToF-AMS was operated under both the "V" and "W" ion optical modes, alternating every 3 min. Under V-mode operation, the AMS cycle through the mass spectrum (MS) mode and the particle time-of-flight (PToF) mode every 30 s, spending 10 s and 20 s, respectively. The HR-ToF-AMS calibrations were conducted following the standard protocols described in previous publications (Jayne et al., 2000; Jimenez, 2003).

Collocated instruments in BJ were as follows: a single-lens ceilometer (CL51, Vaisala, Finland) was used to observe the attenuated backscattering coefficient profiles, and then, the MLH could be calculated according to previous studies (Münkel et al., 2007; Tang et al., 2016; Tang et al., 2015). An MWR (RPG-HATPRO-G5, Germany), number 0030097, was operated simultaneously to obtain the absolute humidity profiles. The MWR produce profiles at 10–30 m resolution up to 0.5 km, 40–70 m resolution from 0.5 km to 2.5 km and 100–200 m resolution from 2 km to 10 km with a temporal resolution of 1 s. A detailed introduction of the MWR can be found in a previous study (Zhao et al., 2019). A ground-based pulsed lidar system, the so-called "WindCube 100s", developed and manufactured by the French company Leosphere, was used in this study. The lidar system was positioned on the ground in the observation field in IAP. Detailed information on the WindCube lidar can be found in a previous study (Cañadillas et al., 2011). Commercial instruments from Thermo Fisher Scientific (TE), USA, were used to measure O_3 (model 49I), $NO/NO_2/NOx$ (model 42I), CO (model 48I), and SO_2 (model 43I). The operational, maintenance, and calibration methods and scheduled quality assurance procedures were previously described in detail (Ji et al., 2014). $PM_{2.5}$ was measured with a TEOM 1405-DF, which is a dichotomous tapered-element oscillating microbalance (TEOM) equipped with a filter dynamics measurement system (FDMS). PM_1 was measured with a TEOM 1405-F, which was equipped with a FDMS. The automatic meteorological observation instruments, Milos520 (Vaisala, Finland), were used to observe the main meteorological parameters, including pressure, temperature, humidity, precipitation, and wind speed and direction in the atmosphere at the ground level. Solar radiation (305–2800 nm) was measured using a CM-11 pyranometer (Kipp & Zonen, Delft, Netherlands) with an accuracy of 2–3%, which was installed on a flat platform on the roof (at an altitude of approximately 10 m) of the IAP (Hu et al., 2011).

The Q-AMS (Aerodyne Research Inc., Billerica, MA, USA) and collocated instruments were deployed at the Xinglong Atmosphere Background Observation Station of the Chinese Academy of Sciences. A detailed instrumental description of Q-AMS can be found in previous studies (Canagaratna et al., 2007; Jayne et al., 2000; Xu et al., 2016; Y. Zhang et al., 2014). The collocated measurements included NR-PM_1 species by the Q-AMS, gaseous pollutants (O_3, NO, NO_2, CO, and SO_2) by gas analyzers (Thermo Scientific), the MLH by a single-lens ceilometer (CL51, Vaisala, Finland), meteorological parameters (pressure, temperature, humidity, precipitation, and wind speed and direction) by Milos520 (Vaisala, Finland), solar radiation by a CM-11 pyranometer (Kipp & Zonen, Delft, Netherlands), and total PM_1 concentration by a Sharp-5030. The sampling setup and operations in XL were similar overall to those in BJ. The HR-AMS and Q-AMS were calibrated by sampling monodispersed 300-nm dried pure ammonium nitrate particles in the AMS. We generated ammonium nitrate particles with an aerosol atomizer (3076, TSI Inc., USA) and selected them with a differential mobility analyzer (DMA, model 3081, TSI Inc., USA). Based on the standard methods for IE calibrations in Jimenez's (2003) research, we obtained the IE values using calibration processes in XL and BJ, respectively. Before the current study, HR-AMS and Q-AMS were first deployed from October 18 to 27, 2018 at the same site to evaluate the uncertainties between the two instruments. All PM_1 species measured by Q-AMS were highly correlated with those measured by HR-ToF-AMS ($R^2 > 0.9$), while the regression slopes of Q-AMS against HR-AMS varied from 0.83 to 1.21 (Fig. S1). Q-AMS was found to have a larger uncertainty in terms of PM_1 species quantification so that PM_1 species measured by the Q-AMS in XL were further corrected by the regression slopes of the Q-AMS/HR-AMS, which were obtained from the intercomparison study.

2.3. Data analysis

The HR-ToF-AMS data were analyzed by SQUIRREL (v1.57H), PIKA (v1.16H) (DeCarlo et al., 2006), and the PMF2 algorithm (Paatero and Tapper, 1994) in PET (v3.04A; (Ulbrich et al., 2009)) in Igor Pro 6.37 (Wave-Metrics Inc., Lake Oswego, OR). The relative ionization efficiency (RIE) values used in XL and BJ were 1.2, 1.1, 1.3, and 1.4 for sulfate, nitrate, chloride, and OA, respectively. RIE values of 4.0 were used for ammonium based on the IE calibration results both in XL and BJ.

CE was introduced to correct the incomplete detection of aerosol particles. Middlebrook et al. (2012) recently suggested that the CE should be composition-dependent with influences of (1) high nitrate content, (2) high relative humidity, and (3) high acidity, implying that the CE should depend on the phase state (liquid or solid) of the particles. In this study, the aerosol particles were dried by a silica gel diffusion dryer before sampling in the vacuum system, and the submicron aerosols were almost neutralized in XL and BJ. Therefore, the impacts of high acidity and high RH on the CE value were limited. However, the ammonium nitrate mass fractions (ANMF) in XL and BJ were normally

above 0.4, especially in XL, indicating that NH_4NO_3 would substantially affect CE. Therefore, the CE value cannot be 0.5. The CE values in XL and BJ were calculated as follows according a previous research (Middlebrook et al., 2012):

$$CE = \max(0.45, 0.0833 + 0.9167 * ANMF) \text{ (Middlebrook et al., 2012)}$$

Positive matrix factorization (PMF) with the PMF2.exe (v3.04) algorithm (Paatero and Tapper, 1994) was used to analyze the HR-AMS and Q-AMS organic spectral matrices following the procedures reported in Ulbrich et al. (2009). More detailed PMF diagnostics are presented in the supplementary materials. PMF analysis of the high resolution mass spectrum (HRMS) in BJ identified six OA factors, including four primary OA (POA) factors from traffic (HOA), coal combustion (CCOA), cooking (COA), biomass burning (BBOA) and two secondary OA (SOA) factors, including less oxidized SOA (LO-OOA) and more oxidized SOA (MO-OOA). PMF analysis of Q-AMS organic spectra in XL resolved a POA factor and a SOA factor. These OA factors were distinguished by their unique signatures in mass spectral patterns and diurnal variations. More detailed PMF diagnostics are presented in the supplementary materials (Figs. S3–4). To better compare the OA in XL and BJ, the four factors in BJ, i.e., HOA, COA, CCOA, and BBOA, were recombined into one POA factor, and the two factors of LO-OOA and MO-OOA were recombined into one SOA factor.

2.4. Backward trajectory modeling and potential source contribution function (PSCF)

Air masses related to local or regional meteorological conditions could be responsible for the atmospheric transport of aerosol particles in the vertical and horizontal directions. Pollution cases in BJ and XL caused by air mass transport from various directions could be quite different. The HYSPLIT4.9 model from the (NOAA) Air Resources Laboratory (available online: http://ready.arl.noaa.gov/HYSPLIT.php) and meteorological data (GDAS for $1° \times 1°$ resolution) were used to calculate the individual 24-hour backward trajectories. The 24-hour air mass back trajectories were calculated by the HYSPLIT model at heights of 100 m, 200 m, and 500 m (above ground level) at the sample site in BJ (39°58′N; 116°22′E; 45 m a.s.l.) and at 1100 m, 1200 m, and 1500 m (above sea level) at the sample site in XL (40°24′N; 117°40′E; 960 m a.s.l.).

To investigate and quantify the effects of regional transport on the PM_1 species in BJ and XL, the PSCF receptor models were used, which was based on the results of the HYSPLIT model and the concentrations of PM_1 species. A detailed description can be found in Wang et al. (2009). Briefly, the ij_{th} component of a PSCF field can be obtained as follows:

$$PSCF(i, j) = m_{ij}/n_{ij}$$

where n_{ij} is the total number of end points that fall in the ij_{th} cell, and m_{ij} is the number of endpoints of that parcel for which the measured values exceed a user-determined threshold criterion. According to previous studies at urban and rural sites, the 75th percentile of PM_1 species was used as the threshold value to m_{ij}. The domain for the PSCF was set in the range of (30–55°N, 95–125°E) with a grid cell size of $0.5° \times 0.5°$. Higher PSCF values indicate higher potential source contributions to the receptor site. Notably, cells with few endpoints may result in high uncertainty in the PSCF method. Thus, to remove these high uncertainties, a weighting function $W(n_{ij})$ recommended by Polissar et al. (1999) was multiplied into the PSCF value:

$$W(nij) = \begin{cases} 1.00 & 80 < nij \\ 0.70 & < nij \le 80 \\ 0.42 & < nij \le 20 \\ 0.05 & nij \le 10. \end{cases}$$

3. Results and discussion

3.1. Mass concentrations and chemical compositions

The variations in PM_1 concentrations are altered between clean periods and haze episodes in both BJ and XL, which is consistent with previous observations in winter in the NCP region (Zhu et al., 2016). As shown in Fig. 2(d), the ratio of BJ to XL (BJ/XL) for daily average PM_1 concentration was larger than 1 most of the time, which indicated that the PM_1 level in BJ was mostly higher than that in XL. The average concentration of PM_1 in BJ (26.6 ± 31.7 μg m^{-3}) was 66% higher than that in XL (16.0 ± 18.7 μg m^{-3}). The correlation coefficient of the average daily PM_1 concentrations in BJ and XL was approximately 0.7, which indicated a relatively strong regional characteristic of aerosol pollution in the NCP. However, the ratio of BJ to XL for PM_1 varied dramatically from 0.44 to 5.58 (Fig. 2(d)). As shown in Fig. S2, XL shows obviously higher frequencies of high wind speed (>2 m/s) and relatively high mixing layer height (MLH) (400–1600 m) than those in BJ. In addition, XL shows obviously lower frequencies of calm wind (<0.2 m/s) than that in BJ. The average wind speed (2.5 m/s) and MLH (739 m) in XL is higher than that in BJ (1.2 m/s, 636 m), indicating better diffusion conditions in both the vertical and horizontal directions in XL. Meanwhile, XL shows higher frequencies in terms of both south and southwest winds than that in BJ, suggesting stronger regional transportation in XL from the south and southwest regions. In addition, XL shows higher frequencies of moderately low RH (20–40%) than that in BJ, yet the frequencies of high T (>0 °C) are lower. Such meteorological differences are among the major reasons leading to the different frequency distributions of PM_1 between BJ and XL (Fig. S2(a)). For example, the periods with low PM_1 levels (<20 μg m^{-3}) account for much more time in XL than in BJ (78% vs. 55%), which is due to the better diffusion conditions in XL. XL shows a lower frequency, and the frequency distributions change dramatically in the PM range above 80 μg m^{-3}, suggesting that heavy pollution is relatively rare in XL.

As shown in Fig. 2(e, f), the aerosol bulk compositions in XL and BJ are obviously different. The aerosol composition in XL showed a lower contribution of organic aerosol (33% vs. 43%) than in BJ Nitrate is the most abundant inorganic species at both sites, accounting for 30% of PM_1 in BJ and 35% in XL, suggesting an important role of nitrate in PM pollution at both urban and background sites in the NCP. In contract, the contributions of sulfate to PM_1 were 12% both in BJ and XL, which were obviously lower than that in nitrate. Recent studies have indicated the increasing role of nitrate in winter haze pollution in BJ (Chen et al., 2018; Li et al., 2019; W. Xu et al., 2019). For example, Li et al. (2019) showed that the nitrate contribution to PM_1 increased from 19% to 32% from 2014 to 2017 winter, while that of SO_4 remained relatively unchanged. Such a phenomenon that ammonium nitrate shows an increase due to reduction in SO_2 emissions has been observed previously in North-Western Europe (Morgan et al., 2010). Indeed, SO_2 concentrations were low both in XL (1.8 ± 1.9 ppb) and BJ (2.7 ± 2.5 ppb; Table 1). Except for the influence of regional transport, the higher proportion of nitrate in XL is also partly attributed to local chemical production because of the high ozone (O_3) concentration, low nitric oxide (NO) concentration and moderate nitrogen dioxide (NO_2) concentration (Table 1). Overall, these differences in the chemical compositions of PM_1 discussed above between BJ and XL may be attributed to different emissions, meteorological conditions, and secondary formation mechanisms.

3.2. OA source appointment

PMF analysis was used to analyze the data of two periods in both BJ and XL, from November 11 to 28, 2018, February 5 to 31, 2019, respectively. PMF analysis of the HRMS in BJ identified six OA factors, including hydrocarbon-like OA (HOA), cooking-related OA (COA), coal combustion OA (CCOA), biomass burning OA (BBOA), less oxidized SOA (LO-

Please cite this article as: J. Li, Z. Liu, L. Cao, et al., Highly time-resolved chemical characterization and implications of regional transport for submicron ..., Science of the Total Environment, https://doi.org/10.1016/j.scitotenv.2019.135803

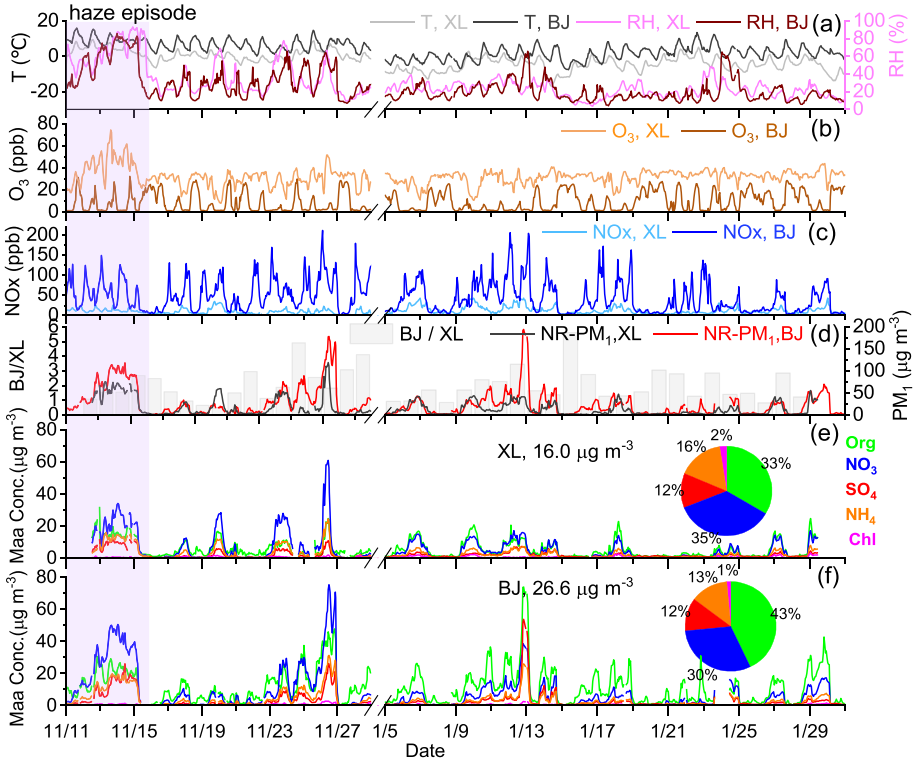

Fig. 2. Time series of (a) relative humidity (RH) and temperature (T), (b) Ozone (O_3) concentration, (c) Oxynitride (NOx) concentration, (d) NR-PM_1 concentrations and the ratio of BJ to XL for daily average PM_1 concentration, (e) NR-PM_1 species in XL, and (f) PM_1 species in BJ. The pie charts depict the average chemical composition in XL and BJ, respectively.

OOA) and more oxidized SOA (MO-OOA) (Fig. 3(a, b)). Detailed mass spectrums and diagnostic information for this PMF solution can be found in the supplementary materials (Figs. S3(a, b), S4).

Table 1
Summary of average meteorological parameters, gaseous precursors, and NR-PM_1 species in Xinglong (XL) and Beijing (BJ). The data are listed in the form of "average ± standard deviation".

	XL	BJ
Meteorological parameters		
T (°C)	−2.4 ± 4.7	3.6 ± 4.5
RH (%)	29 ± 18	26 ± 17
WS (m s^{-1})	2.5 ± 1.1	1.2 ± 0.9
P (Hpa)	918 ± 3	1020 ± 5
SR (W m^{-2})	103 ± 176	89 ± 153
MLH (m)	744 ± 395	639 ± 442
Gaseous precursors		
O_3	32 ± 8	9 ± 8
NO	2 ± 1	24 ± 30
NO_2	10 ± 8	21 ± 11
NOx	12 ± 8	45 ± 38
SO_2	1.8 ± 1.9	2.7 ± 2.5
CO	0.6 ± 0.4	0.8 ± 0.6
Aerosol species/μg m^{-3}		
Org	5.4 ± 5.2	11.5 ± 10.6
POA	2.2 ± 1.9	6.7 ± 6.6
HOA		1.3 ± 1.4
COA		2.4 ± 2.7
BBOA		1.3 ± 1.7
CCOA		1.7 ± 2.1
SOA	3.2 ± 3.6	4.7 ± 4.9
LO-OOA		1.6 ± 1.0
MO-OOA		3.2 ± 4.1
SO_4	1.9 ± 2.3	3.2 ± 5.7
NO_3	5.6 ± 8.5	8.2 ± 12.1
NH_4	2.6 ± 3.6	3.5 ± 5.1
Cl	0.4 ± 0.5	0.4 ± 0.5
NR-PM_1	15.7 ± 18.7	26.6 ± 31.7

The MS of HOA was mainly composed of hydrocarbon ions $C_nH_{2n+1}^+$ (*m/z* 29, 43, 57) and $C_nH_{2n-1}^+$ (*m/z* 27, 41, 55), which are common primary combustion emissions (J. Zhang et al., 2014; Zhang et al., 2016). The correlation coefficients of HOA and NOx were 0.58 and 0.56, indicating that HOA was mainly emitted from traffic source emissions, namely, diesel truck and gasoline car exhaust (Y.L. Sun et al., 2010; Zhang et al., 2005). The diurnal pattern of HOA (Fig. S4) further confirmed the association of HOA with traffic activities, as this pattern showed two obvious peaks during morning and evening rush hours.

The MS of COA was characterized by higher f55 and f57 (mass fraction of *m/z* 55 and 57 in OA) values, and the ratio of *m/z* 55/57 in the MS of COA was high (~2.4) and close to the values reported in previous studies in Beijing (J. Sun et al., 2010; Zhao et al., 2017). The diurnal pattern of COA showed a pronounced diurnal cycle with two prominent peaks (Fig. S4), in accordance with the lunch and dinner times of the pollutant residents.

The MS of CCOA was characterized by prominent contributions of unsaturated hydrocarbons, especially PAH-related ion peaks (e.g., 77, 91, and 115) (Huang et al., 2018). The temporal trend of CCOA correlated well with that of *m/z* 115 ($R^2 = 0.81$) and PAH ($R^2 = 0.87$) from November 11 to 30, 2018. The correlation coefficients of CCOA and *m/z* 115, PAH were 0.92 and 0.93, respectively, from February 5 to 31, 2019. All these characteristics were consistent with previous studies in Beijing (Hu et al., 2016). In addition, the CCOA showed distinct diurnal variations with low concentrations during the day and high concentrations at night, indicating relatively strong emissions from residential heating activities (Fig. S4). The average fraction of CCOA to OA accounted for 14%, which was obviously reduced compared with Hu et al.'s (2016) and J. Zhang et al. (2014) results in the 2010 and 2013 winters in Beijing, and the concentration also decreased rapidly, indicating an effective reduction of combustion in the Beijing area due to the coal to gas project.

The MS of BBOA was characterized by prominent peaks at *m/z* 60 and 73 (Fig. S3(a, b)), which are two indicative tracers of biomass burning (Aiken et al., 2009; Hu et al., 2017; Lee et al., 2010). BBOA correlated

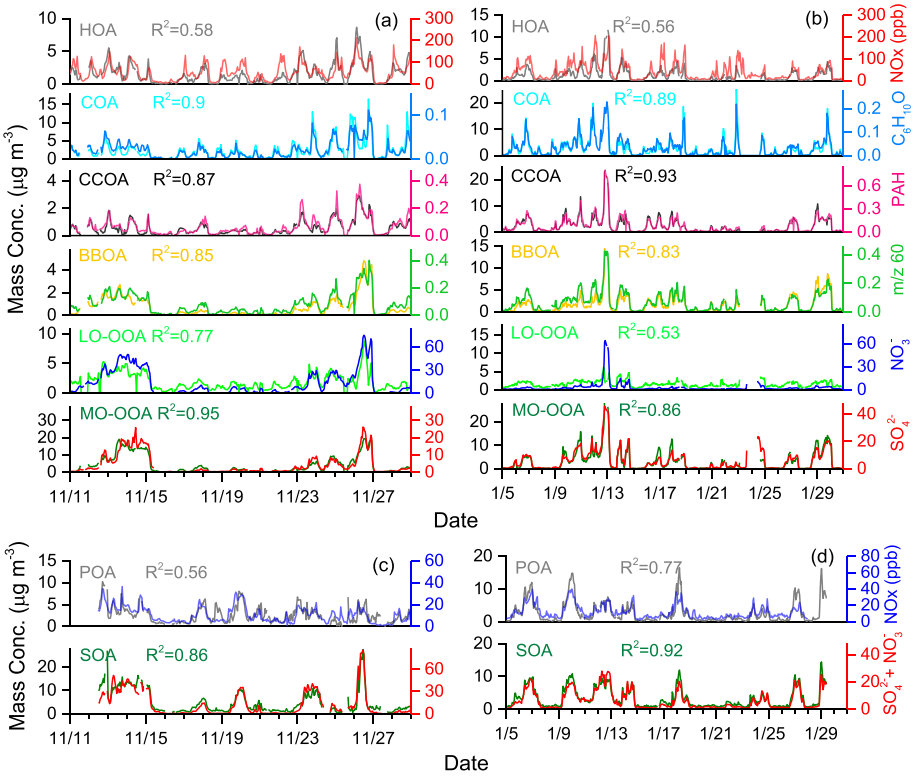

Fig. 3. Time series of six organic aerosol (OA) factors in BJ (a, b): hydrocarbon-like OA (HOA), cooking-related OA (COA), coal combustion OA (CCOA), biomass burning OA (BBOA), less oxidized oxygenated OA (LO-OOA), and more oxidized OOA (MO-OOA). The time series of NOx, $C_6H_{10}O^+$, PAH, *m/z* 60, nitrate, and sulfate are shown for comparison. Time series of two OA factors in XL (c, d): primary OA (POA) and secondary OA (SOA). The time series of NOx, nitrate, and sulfate are shown for comparison.

well with *m/z* 60 and showed similar diurnal variations with those of CCOA. The O/C of BBOA was 0.33 and 0.28, which was thought to be contributed by oxygenated species from biomass burning, as these results were close to those of previous studies (Hu et al., 2016).

Oxygenated fragments ($C_xH_yO_z^+$) are prominent in the MS of OOA. In this study, the MS of OOA was characterized by a dominant peak at *m/z* 44 (mainly CO_2^+), in accordance with many previous studies (Huang et al., 2010; Zhao et al., 2017). Because the volatility of OOA cannot be directly measured in the experiment, many previous studies in Beijing classified OOA into two categories based on the O/C value: less oxidized oxygenated SOA (LO-OOA) and more oxidized oxygenated SOA (MO-OOA) (Xu et al., 2017; Zhao et al., 2017; Li et al., 2020). Two OOA factors were identified in the study. LO-OOA and MO-OOA were both characterized by high f44 (mass fraction of *m/z* 44 in OA) values. The f44 value in MO-OOA was higher than that in LO-OOA, while f43 in MO-OOA was lower than that in LO-OOA. In addition, the O/C ratio of MO-OOA was up to 1.09 and 1.06, which was much higher than that of LO-OOA (0.61, 0.78; Fig. S3(a, b)). All these characteristics indicated that MO-OOA was more oxidized than LO-OOA. MO-OOA correlated well with sulfate and nitrate ($R^2 = 0.95$ and 0.86, respectively).

The PMF analysis of Q-AMS organic spectra in XL resolved a POA factor and a SOA factor (Fig. S3(c, d)). The MS of POA was mainly composed of hydrocarbon ions $C_nH_{2n+1}^+$ (*m/z* 29, 43, 57) and $C_nH_{2n-1}^+$ (*m/z* 27, 41, 55), which was similar to the MS of HOA in BJ (Fig. S3(c, d)). The coefficients of HOA and NOx were 0.56 and 0.77, indicating that HOA was mainly emitted from traffic source emissions. In addition, the PAH-related ion peaks (e.g., *m/z* 77, 91, and 115) (Huang et al., 2018) and the indicative tracers of biomass burning (Aiken et al., 2009; Hu et al., 2017; Lee et al., 2010) (*m/z* 60 and 73) also accounted for approximately 1% of OA, indicating that coal combustion and biomass burning also partly contribute to POA in XL. The MS of SOA in XL was dominated by *m/z* 44 (Fig. S3(c, d)), in accordance with many previous studies (Huang et al., 2010; Zhao et al., 2017). SOA correlated well with sulfate and nitrate ($R^2 = 0.86$ and 0.92, respectively).

In summary, PMF analysis of HRMS in BJ identified six OA factors, including four POA factors (HOA, CCOA, COA, and BBOA) and two SOA factors (LO-OOA and MO-OOA). However, PMF analysis of Q-AMS organic spectra in XL resolved a POA factor and a SOA factor. To compare the OA in XL and BJ better, the four primary factors and two secondary factors in BJ were recombined into one POA factor and one SOA factor. Overall, the average concentration of POA in BJ (6.7 μg m^{-3}) was 68% higher than that in XL (2.2 μg m^{-3}), while the average concentration of SOA in BJ (4.7) was only 28% higher than that in XL (3.2 μg m^{-3}). Meanwhile, SOA accounted for 59% of OA in XL, which was higher than that in BJ (42%). These results suggested low primary emissions and highly oxidized OA during the long-range transport in XL. Since there are few anthropogenic emissions in the surroundings of the XL station, this was most likely the result of aerosol transport from urban areas and photochemical and aqueous-phase formation of SOA during transport.

3.3. Diurnal evolution of aerosol species and OA factors

Diurnal variations in meteorological parameters, gaseous precursors, and PM_1 species are shown in Fig. 4. The diurnal variations in meteorological parameters in XL were obviously different from those in BJ. The XL station is located on a mountain with an altitude of 960 m, so the average temperature is lower and the average wind speed is higher than that in BJ. The wind speed in BJ showed obvious diurnal variation, with high values in the daytime and low values at night. However, in XL, the wind speed was at a high level even at night. Meanwhile, the MLH at night was also higher than that in BJ. These characteristics suggest that regional transport may play a significant role in haze pollution in XL. Notably, the total radiation (SR) in XL was obviously stronger, and the peak time occurred at approximately 14:00 and lasted longer, corresponding to the higher O_3 in XL.

The diurnal variations in gaseous precursors in XL were also significantly different from those in BJ. The concentration of NO in XL was much lower than that in BJ. NO_2 showed opposing diurnal variation to

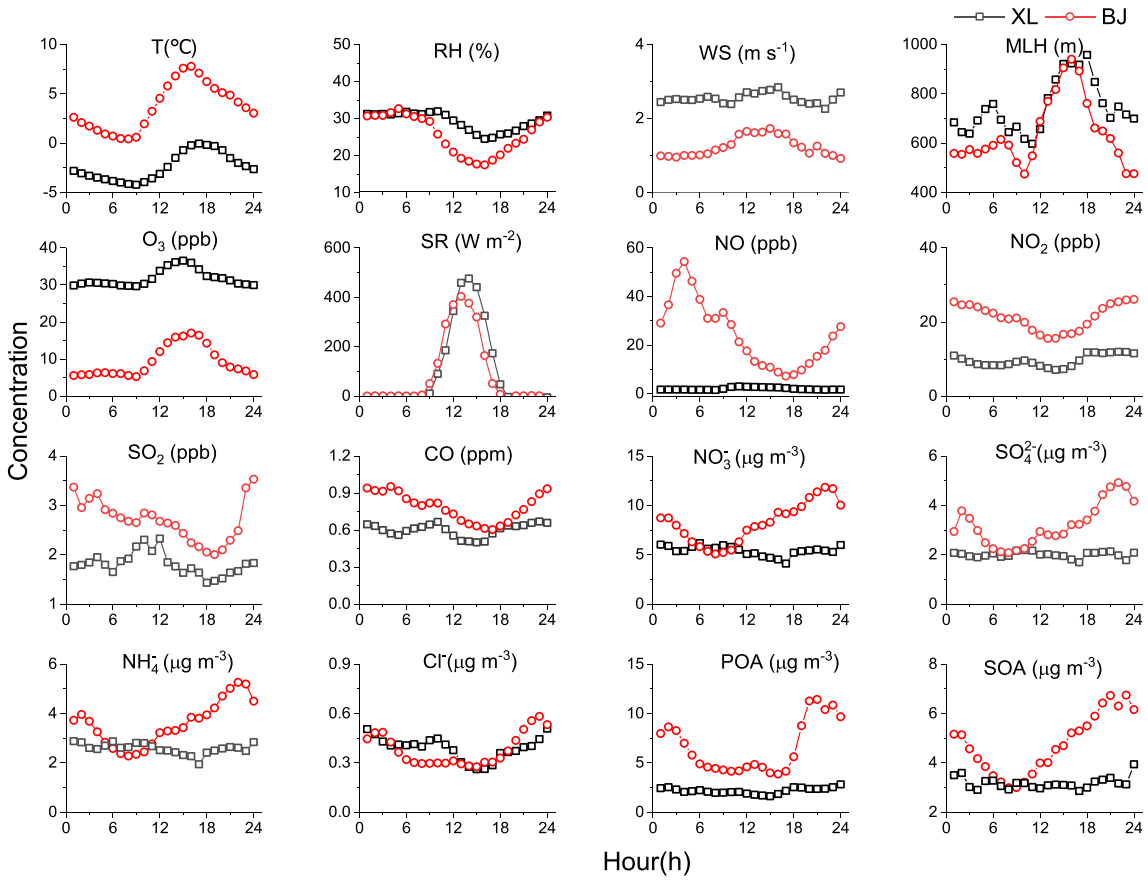

Fig. 4. Diurnal variations in meteorological parameters, gaseous precursors, and PM_1 species in BJ (the red line) and XL (the black line) during the whole observation period (OA: organic aerosol, POA: primary OA, SOA: secondary OA). (For interpretation of the references to colour in this figure legend, the reader is referred to the web version of this article.)

that of O_3, characterized by high concentration at 10:00 and 18:00 and low concentration during daytime hours in XL, and these findings were consistent with the results of a previous study in XL (Wang et al., 2013). The O_3 concentration in XL is obviously higher than in BJ, which is consistent with previous studies that found that O_3 levels in rural sites are higher than in urban sites because of the deterioration of O_3 for high NO levels of urban areas (Keuken et al., 2009; Paoletti, 2009). The high O_3 levels during the daytime in XL can be explained by incoming solar irradiation, which intensifies photochemical reactions of O_3 in the region. O_3 in XL is high even at night (~28 ppb) because of the low NO concentration.

The diurnal variations in PM_1 species in XL and BJ were quite different, suggesting that the major factors driving the diurnal changes were different at the two sites. Secondary inorganic nitrate showed the largest increase in BJ followed by SOA, sulfate, and ammonium. However, in XL, the secondary species showed stable diurnal variations. Meanwhile, primary inorganic chlorine in XL and BJ showed similar diurnal variations. The increases in nitrate in BJ during daytime were mainly caused by photochemical production (Sun et al., 2013b; W. Xu et al., 2019), and the high concentration at night was suggested to be contributed by the hydrolysis of dinitrogen pentoxide (N_2O_5) (Li et al., 2018). Notably, the nitrate in XL at night was slightly higher than that during the daytime, suggesting that the hydrolysis of N_2O_5 contributed higher concentration at night in XL because of the high O_3 concentration at night and low NO concentration. Sulfate can either be produced from the gas-phase reaction of SO_2 with OH radicals or from heterogeneous or aqueous reactions (H_2O_2/O_3 oxidation or metal catalyzed oxidation) (Dlugi et al., 1981; Wang et al., 2012). As shown in Fig. 4, the diurnal pattern of sulfate in BJ rapidly increased from 17:00 to 22:00 as RH increased, indicating an enhanced heterogeneous or aqueous reaction to sulfate formation, which is consistent with previous studies in Beijing (Liu et al., 2016; Quan et al., 2015). In contrast, a flat diurnal pattern of sulfate was observed in XL, which may suggest a weak local secondary transformation due to the low SO_2 levels. SOA in BJ showed a clear daytime increase in diurnal cycles, which was similar to nitrate, indicating that SOA was predominantly from photochemical production in winter (Ge et al., 2017). The results here are consistent with a recent finding of high OH radical concentrations in winter in BJ (Tan et al., 2018). The high concentration of POA in BJ at night indicates that there is a large amount of primary emissions in BJ at night, such as traffic sources, while the small peak value at noon during the day is associated with cooking sources. The diurnal variation in POA in XL was very gentle, and the proportion of SOA was higher than in BJ, suggesting that the OA in XL was highly oxidized during the long-range transport.

3.4. Chemically resolved PM pollution levels

To explore differences in the regional and local variability in secondary aerosol formation processes at urban and background sites, we compared the compositional differences between BJ and XL at different PM_1 and meteorological variables in this section. Fig. 5 shows the variations in mass concentrations and mass fractions of NR-PM_1 species in XL and BJ as a function of the total NR-PM_1 in BJ. Primary species such as chlorine and POA in BJ increased as a function of PM_1 concentration in BJ, while primary species in XL maintained stable and low concentrations, indicating stronger primary emissions in BJ. Nitrate showed a fast increasing rate both in XL (3.1 μg m^{-3} per 10 μg m^{-3}) and BJ (8.4 μg m^{-3} per 10 μg m^{-3}) when PM_1 < 160 μg m^{-3}, resulting in high nitrate fractions in both BJ and XL, which suggests the enhanced role of nitrate in PM_1 during polluted episodes.

Notably, although the increase rate of nitrate in XL was prominently lower than that in BJ, the fraction (~22–48%) was slightly higher than

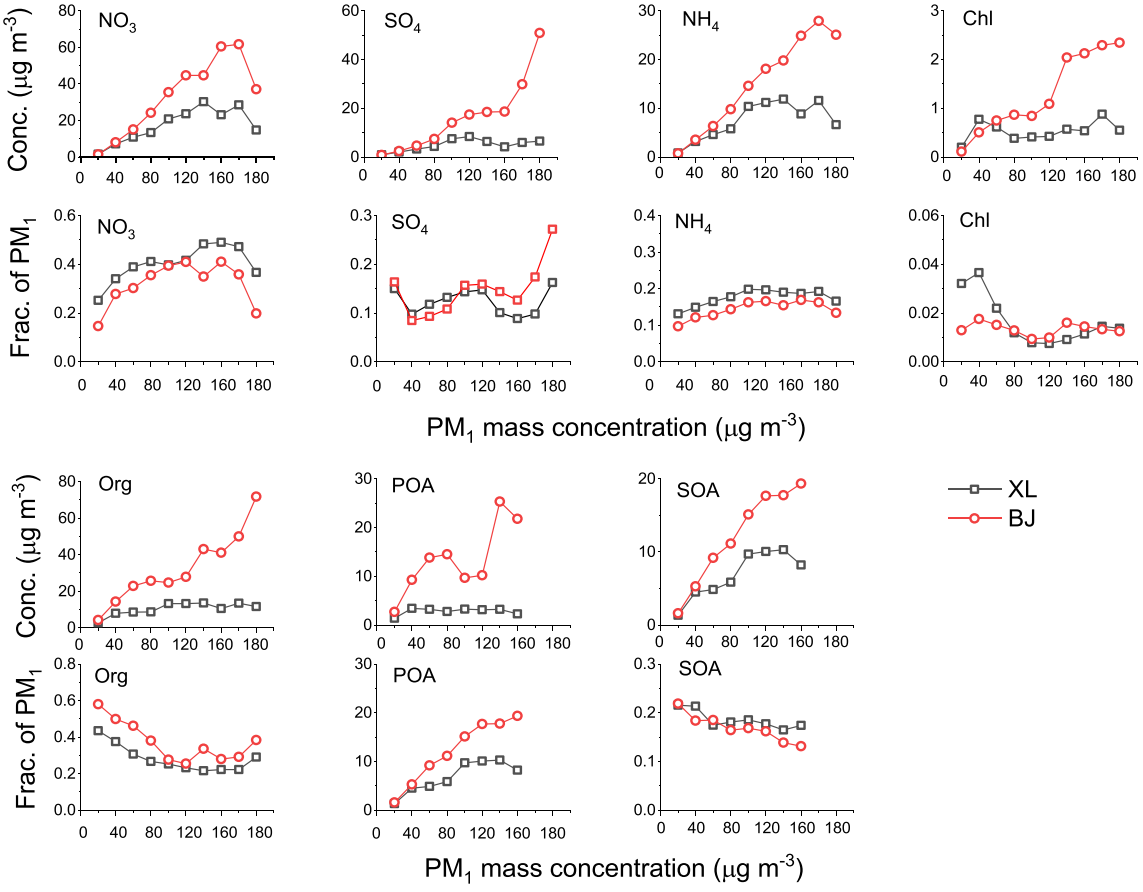

Fig. 5. Variations in mass concentrations and mass fractions of NR-PM_1 species in BJ (red) and XL (black) as a function of the total NR-PM_1 mass loading in BJ. The data are grouped in NR-PM_1 bins in BJ (10-μg m^{-3} increment) (OA: organic aerosol, POA: primary OA, SOA: secondary OA). (For interpretation of the references to colour in this figure legend, the reader is referred to the web version of this article.)

that in BJ (~18–42%). NOx reacts with O_3 to form nitrate radical (NO_3) and N_2O_5 (Prabhakar et al., 2017). Note that the average O_3 concentration at XL was much higher than that in Beijing during nighttime (30 ppb vs. 5 ppb), which may suggest a higher nitrate radical and N_2O_5 formation. The N_2O_5 that formed from the oxidation of NO_2 by NO_3 can be taken up onto aerosols via heterogeneous reactions, which is an important sink of NO_2 and O_3 at night and can compete with the NO_3 reactions with isoprene (Brown et al., 2016; Millet et al., 2016; Xue et al., 2014). Previous studies showed that in remote or high-altitude mountain regions with cleaner air aloft, higher NO_3 levels are often observed (Chen et al., 2011; Sobanski et al., 2016). Thus, the higher nighttime nitrate concentrations in XL could be attributed to the greater efficiency of nitrate radical formation in the background atmosphere and thus enhance nitrate formation. Submicron nitrate mainly exists in the form of semivolatile ammonium nitrate and is produced by the reaction of NH_3 with HNO_3. The formation pathways of HNO_3 include the oxidation of NO_2 by OH during the day and the hydrolysis of N_2O_5 at night (Li et al., 2018). NH_3 tends to react first with H_2SO_4 to form $(NH_4)_2SO_4$ due to its stability, and NH_4NO_3 can be formed when NH_3 is excessive (Seinfeld and Pandis, 2016). During the sampling period, the observed molar ratios of ammonium to sulfate in BJ and XL were larger than 2 (Fig. S5(a, c)), corresponding to an excess of NH_3. The scatter plot of the molar concentration of excess ammonium versus the molar concentration of nitrate indicated that nitrate was usually completely neutralized by excess ammonium (Fig. S5(b, d)). Recent studies have shown that sulfate has been effectively reduced in BJ and that the contribution of nitrate to PM has significantly increased (Li et al., 2019; Xu et al., 2017). The molar ratio of NH_4^+ to SO_4^{2-} increased from 1.5 (before 2013) to 3.33 due to ammonia-rich atmosphere in BJ (Q. Xu et al., 2019). This is mainly because the emission control of coal combustion in BJ and surrounding areas results in an NH_3-rich and SO_2-lean atmosphere, which promotes the formation of ammonium nitrate. Previous studies showed that the ratios (in charge equivalents, $R_{C/A}$) between measured cations (NH_4^+) and anions (SO_4^{2-}, NO_3^- and Cl^-) is a good indicator of aerosol acidity because of the similar temporal trend between $R_{C/A}$ and pH (Tian et al., 2018; Zhou et al., 2018). As shown in Fig. S6(a), when the PM_1 concentration was >80 μg m^{-3}, the average NR values of XL and BJ were 1.09 and 0.94, respectively. The $R_{C/A}$ value in BJ slightly decreased from 1.10 to 0.83 as PM_1 increased from 40 to 180 μg m^{-3}, while the $R_{C/A}$ in XL showed no significant change. The results suggested that the aerosol acidity in BJ was slightly enhanced as PM_1 increased, while in XL, the aerosol acidity remained neutral and thus facilitated nitrate production. This behavior is significant for further emission control measures in BJ. More efforts should be made to reduce the nitrogen oxide and ammonia emissions in BJ and surrounding areas.

The effect of RH on the secondary formation of nitrate was also investigated. As shown in Fig. 6, nitrate increased successively as RH increased in BJ, while in XL, nitrate increased first and then decreased when RH was above 70%. In addition, when RH increased from 40% to 70%, the increase rate of nitrate in XL (6.6 μg m^{-3} per 10%) as a function of RH was similar to that of BJ (7.4 μg m^{-3} per 10%), suggesting the important role of heterogeneous aqueous reaction for nitrate production at both urban and background sites. Notably, the wind speed in XL increased from 2.3 to 2.6 m/s as RH increased from 50% to 70%, while in BJ, the wind speed was below 1 m/s. This behavior indicated that, except for local chemical production, regional transport also played an important role in nitrate concentration in XL. When RH was above 70%, nitrate

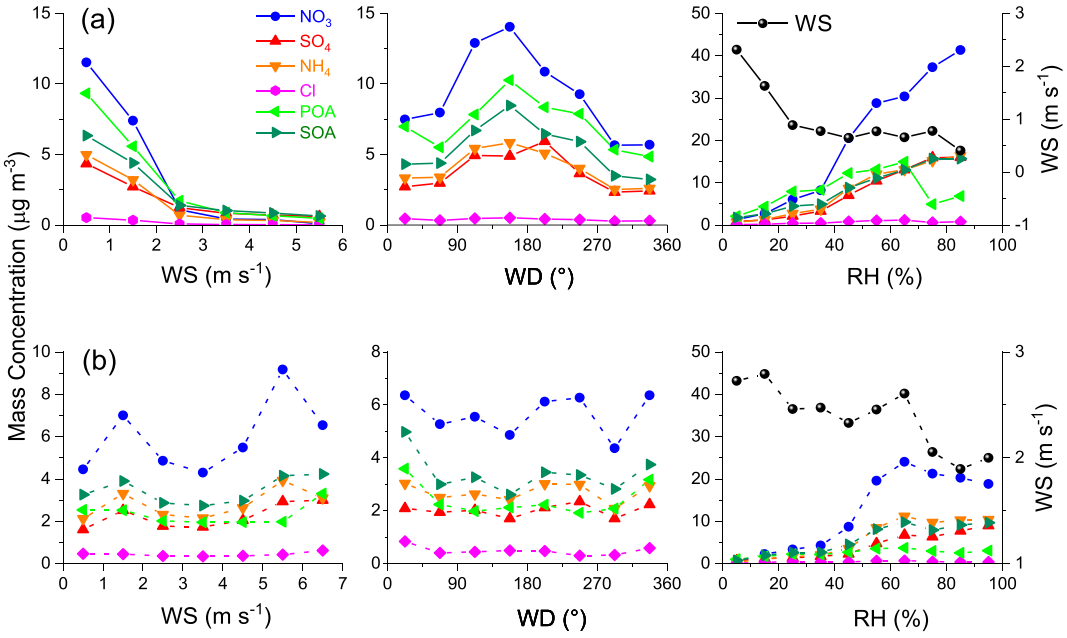

Fig. 6. Variations in mass concentrations and mass fractions of PM_1 species as functions of wind speed (WS), wind direction (WD), and relative humidity (RH) in (a) BJ and (b) XL (OA: organic aerosol, POA: primary OA, SOA: secondary OA).

in XL decreased, and the wind speed also decreased to a low level (~2 m/s) as a function of RH, suggesting the weak influence of regional transport. The variations in nitrate with WS in BJ and XL further prove the significant role of regional transport on nitrate in XL. As shown in Fig. 6, nitrate decreased rapidly as the wind speed increased in BJ, indicating a diluting effect of winds on nitrate concentration. However, nitrate in XL increased significantly from 3 to 6 m/s and showed higher concentration in association with wind from the southwest, although it decreased under the low wind speed conditions (<3 m/s). In addition, the NOR ($=NO_3^- / (NO_3^- + NO_2)$) in XL (Fig. S6(e)) was also slightly higher than that in BJ, especially when PM_1 in BJ increased from 80 to 160 μg m^{-3}, corresponding to an obvious increase in wind speed in XL (Fig. S6(c)). All these characteristics indicated that the more efficiency of regional transport contributed to the relatively higher fraction of nitrate in the background area than in the urban site.

Sulfate increased rapidly in BJ, especially when PM_1 > 160 μg m^{-3} (Fig. 5). In XL, sulfate first increased (PM_1 < 120 μg m^{-3}) and then decreased slightly as PM_1 increased, corresponding to the decrease in RH at the same time (Fig. S6(b)). SOR ($=SO_4^{2-} / (SO_4^{2-} + SO_2)$) showed similar variations to sulfate (Fig. S6(d)), which further proves the importance of heterogeneous reactions for sulfate formation. Sulfate in BJ and XL continuously increased as a function of RH, with an increased rate of 1.8 and 0.9 μg m^{-3} per 10% (Fig. 6), respectively. These results indicated a higher efficiency of secondary transformation of SO_2 by heterogeneous and aqueous-phase reactions in BJ than in XL, which can be attributed to the higher aerosol surface areas due to the higher loading of fine particles at urban sites.

Although SOA shows a faster increasing rate and higher concentration in BJ than XL across different PM_1 levels, the contribution of SOA to PM_1 in XL (~13–21%) are slightly higher than those in BJ (~16–21%) (Fig. 5). SOA in XL decreased rapidly as the wind speed increased from 1 to 3 m/s and then increased significantly from 3 to 6 m/s (Fig. 6). Therefore, the higher concentration of SOA in XL was due to low primary organic emissions and highly oxidized OA during the regional transport. Aqueous-phase processing played a minor role in SOA formation in XL, as the increased rate of SOA in XL (2.4 μg m^{-3} per 10%) was obviously lower than that of nitrate (6.6 μg m^{-3} per 10%) as a function of RH when RH increased from 40% to 70% (Fig. 6).

Because of the significant role of regional transport to aerosols in XL, especially for nitrate and SOA, the PSCF analysis on account of the HYSPLIT model was used to identify the potential source regions of the PM_1 species in BJ and XL. Fig. S7 shows the PSCF map produced using the daily contribution date with the 75th percentile cut of each source factor. High potential source areas were mainly located to the south and southwest of BJ (Fig. S7(a)), highlighting the important role of regional transport from these regions to aerosol concentration in BJ. We also noticed different potential source regions for different aerosol species. For example, the source regions of secondary PM_1 species, such as nitrate, sulfate, ammonium, and SOA, were mainly located in the south and southwest of BJ. POA had a relatively small potential source region in the south of BJ and a high source region located around and in the area west of BJ. The potential source regions of aerosol species in XL (Fig. S7(b)) were similar to those in BJ. High potential source areas for all kinds of PM_1 species were mainly located in the southwest (including the location of BJ) areas of XL. These results indicate the significant role of regional transportation from the southwest regions to the elevation of secondary aerosols in both BJ and XL. Moreover, urban BJ could also be recognized as an important potential source region of aerosols in the background area of XL.

3.5. Case studies for the formation mechanism of regional haze episode

The above analysis showed that the southwest regions in the NCP were the main source area of secondary aerosols in both BJ and XL. Therefore, a typical episode with air masses from southwest regions was selected to study the aerosol formation mechanisms in the two sites and the favorable conditions for aerosol transport from BJ to XL. Previous studies have showed that factors affecting regional haze formation vary during different pollution periods (Zhu et al., 2016; Huang et al., 2017). To improve our understanding of haze formation on a regional scale, we divided the regional haze episode into four stages: clean period I on 11 November (I), the transition period from 12 to 13 November (II), the polluted period on 14 November (III), and clean period II on 15 November (IV) (Fig. 7). This type of classification method has been mentioned in previous studies (Zhu et al., 2016; Guo et al., 2014), and the corresponding terms in the present study have the same definition.

Please cite this article as: J. Li, Z. Liu, L. Cao, et al., Highly time-resolved chemical characterization and implications of regional transport for submicron ..., Science of the Total Environment, https://doi.org/10.1016/j.scitotenv.2019.135803

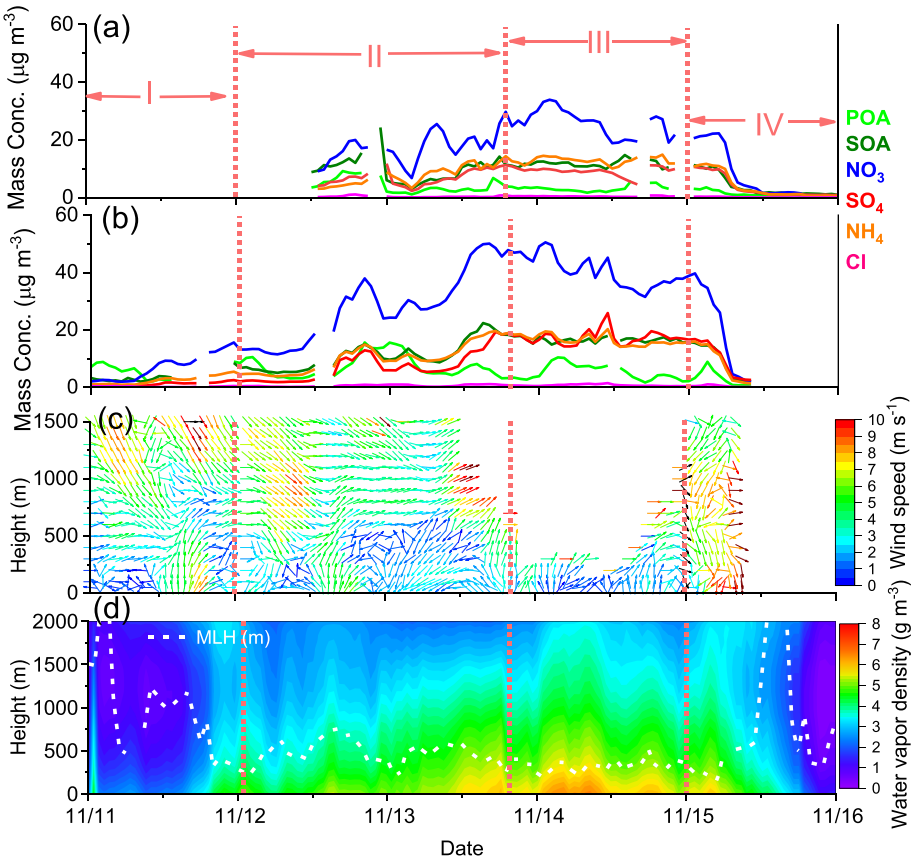

Fig. 7. Temporal evolution of (a) PM_1 species in XL, (b) PM_1 species in BJ, (c) horizontal wind vector profiles, (d) water vapor density profiles and atmospheric mixing layer height (MLH) in BJ.

The transition period describes the shift from a clean period to a polluted period. During the transition period (II) of the haze episode in BJ, the southerly wind prevailed throughout the Beijing-Tianjin-Hebei region at both ground and 850-hPa geopotential height (Fig. S8(a, b, c); Fig. S9(a, b, c)). Back trajectories also showed air masses from the southwest arriving in BJ (Fig. S10(a, b, c)). During the same period, according to the horizontal wind vector profiles shown in Fig. 7(c), southerly winds prevailed in BJ from November 11 afternoon to 13 afternoon in the MLH. Considering the heavily populated industrial regions in the south of BJ (Z. Liu et al., 2019), south winds can carry heavy anthropogenic aerosols to BJ, which mainly caused the rapid increase in PM_1. The PM_1 mass concentration rapidly increased from less than ~40 to ~90 μg m^{-3} in the afternoon of November 12 and from ~60 to 110 μg m^{-3} in the afternoon of November 13 (Fig. 7(b)). The hourly growth rates of nitrate in BJ in the afternoon of November 12 and 13 were 2.6 and 3.3 μg m^{-3} h^{-1}, respectively. As shown in the horizontal wind field superimposed on the background 850-hPa specific humidity field (Fig. S9(a, b, c)), a week moisture transport belt formed under the action of the horizontal wind field, through which water vapor from southern China was constantly being carried to BJ. This behavior could explain the sudden increase in water vapor density to ~4 g m^{-3} in the MLH (Fig. 7(d)), which is consistent with a previous study that the southerly transport of water vapor in the upper mixing layer in the initial stage of pollution led to a gradual increase in regional RH (Zhu et al., 2016).

During the transition period (II) of the haze period in XL, the haze episode was also caused by strong southern regional transport. Weather maps and wind fields at the 850 hPa geopotential height (Fig. S9(a, b, c)) showed that BJ and XL (960 m a.s.l.) were located behind the high-pressure anticyclone, which made the dominant winds in XL south winds, with a moderate wind speed, reaching ~3 m/s. Furthermore, the southwest wind in BJ appeared from the surface to ~1100 m and even stronger in the layer of 700 to 1100 m, which transported the pollutants from BJ toward the downwind (northwest) regions (Fig. 7(c)). In addition, back trajectories also showed air masses from the southwest arriving in XL from BJ at 08:00 on November 13 (Fig. S10(f)), indicating the transport of air masses from BJ to XL in the afternoon of November 12. Correspondingly, the rapidly increasing PM_1 concentration in XL (960 m a.s.l.) was observed simultaneously above the downwind area (Fig. 7(a)), exactly in response to the continuous and intensive southwesterly winds. From 12:00 to 20:00 on November 12, the concentrations of nitrate and SOA increased from 12.4 to 24.0 μg m^{-3} and from 8.8 to 15.4 μg m^{-3}, respectively (Fig. 7(a)). Therefore, the original explosive growth in nitrate and SOA in XL was associated with southwestern transportation from BJ. Similarly, the rapid PM_1 increase in the afternoon of November 13 in XL was also caused by regional transport from southern regions.

During the polluted period (III) in BJ, although a weak south wind still exists in the MLH, the impact of regional transport decreased because of stable stratification in the MLH (lower than 500 m) and local secondary formation enhanced by heterogeneous reactions. The secondary formation of sulfate, nitrate, and ammonium is related to heterogeneous aqueous reactions and largely depends on RH (Quan et al., 2015). Pollutants in BJ were trapped in the low MLH; thus, the transport of pollutants from BJ to XL decreased during the polluted period. Although the transport of pollutants from BJ to XL decreased, the water vapor transport belt at 850 hPa increased from southern areas to XL with continuous moderate south winds and specific humidity on November 14 (Fig. S9(d, e, f)). Therefore, a large amount of water vapor was transported to XL from southern China in the later period of the haze episode, with a rapid increase in RH, reaching ~90% in XL. As expected, the already high PM_1, nitrate, sulfate, and ammonium values

in XL showed slightly increasing trends in the polluted period and maintained high values of ~60 μg m^{-3}, ~26 μg m^{-3}, ~10 μg m^{-3} and 13 μg m^{-3}, respectively (Fig. 7(a)). Therefore, the transport of water vapor from southern China enhanced secondary aerosol formation in XL. Compared to XL, the water vapor at the 850 hPa geopotential height could not reach the ground in BJ because of the low MLH (below ~500 m). Notably, a rapid boost in atmospheric humidity with a water vapor density of ~6–8 g m^{-3} expanded throughout the entire MLH (Fig. 7(d)). This rapid increase in humidity was attributed to the compression of the MLH because of the higher water vapor density on the ground (Fig. 7(d)), which was verified by previous comprehensive studies of observations and simulations (Q. Liu et al., 2018; Zhu et al., 2016).

Overall, during the transition period of the regional haze episode, the enhanced southwest wind transported pollutants to the downwind area. The explosive growth of nitrate and SOA in XL was the result of southwestern transportation from BJ. During the polluted period, pollutants transport from BJ to XL decreased because of the low MLH in BJ, while the water vapor transport belt at 850 hPa was enhanced from the southern areas and favored the secondary formation of aerosols in XL. Unlike in XL, a rapid increase in the water vapor density in BJ was due to the compression of the MLH.

4. Conclusion

An HR-AMS and a Q-AMS were deployed at an urban site in BJ and a background site in XL in the NCP, respectively. The results are as follows: the average mass concentrations of PM_1 in BJ and XL were 26.6 ± 31.7 and 16.0 ± 18.7 μg m^{-3} during the observation period, respectively. The ratio of BJ to XL (BJ/XL) for PM_1 varied dramatically from 0.44 to 5.58, and the aerosol composition in XL showed a lower contribution of OA (33% vs. 43%) and higher fractions of nitrate (35% vs. 30%), ammonium (16% vs. 13%), and chlorine (2% vs. 1%) in XL than in BJ. PMF analysis of the HRMS in BJ identified six OA factors, including four POA factors from traffic (HOA), coal combustion (CCOA), cooking (COA), biomass burning (BBOA) and two SOA factors, including LO-OOA and MO-OOA. In XL, a POA factor and a SOA factor were identified. SOA accounted for 59% of OA in XL, which was higher than that in BJ (42%), suggesting low primary emissions and highly oxidized OA during the long-range transport in XL. These differences were caused by different emissions, meteorological conditions, and secondary formation mechanisms.

The diffusion condition in XL is better than in BJ. The O_3 concentration in XL is higher than in BJ even at night (~30 ppb) because of the low NO and moderate NO_2 concentrations, which may favor nighttime nitrate formation in XL. In both BJ and XL, nitrate displayed a significantly enhanced contribution with the aggravation of aerosol pollution, which was completely neutralized by excess ammonium at both sites, suggesting that the abundant ammonia emissions in the NCP favor nitrate formation on a regional scale. A higher proportion of nitrate in XL can be attributed to the more neutral and higher oxidation capacity for the background atmosphere and a more significant impact of regional transport on the background site. Heterogeneous aqueous reaction plays an important role in the enhanced formation of nitrate in both XL and BJ because of the similar increase rate of nitrate in XL (6.6 μg m^{-3} per 10%) and BJ (7.4 μg m^{-3} per 10%) as a function of RH when RH increased from 40% to 70%. However, for sulfate and SOA, heterogeneous aqueous reaction plays a more important role in BJ than in XL, which can be attributed to the higher aerosol surface areas due to the higher loading of fine particles at urban site.

The PSCF results show that the southwest region is the main source area of secondary aerosols in both BJ and XL. Therefore, a typical episode with air masses of BJ and XL from the southwest direction was chosen for further study. Both XL and BJ are heavily polluted with a high contribution of secondary aerosol particles. During the transition period, the enhanced southwest wind from near the surface to 1.1 km in BJ transported pollutants from BJ to XL (the downwind area), which resulted in the rapid increase in nitrate and SOA in XL over a short time. During the polluted period, the pollutants transported from BJ to XL decreased because of the low MLH in BJ, while the water vapor transport belt at 850 hPa was enhanced from southern areas and favored the secondary formation of aerosols in XL. Unlike in XL, a rapid increase in the water vapor density in BJ was due to the compression of the MLH. The enhanced pollutant transport during the transition pollution stage and the enhanced water vapor transport in the polluted pollution stage to the downwind background areas expanded the regional scope of the haze in the NCP.

Declaration of competing interests

The authors declare that they have no known competing financial interests or personal relationships that could have appeared to influence the work reported in this paper.

Acknowledgements

This study was supported by the Ministry of Science and Technology of China (Grant nos. 2017YFC0210000), the National Natural Science Foundation of China (Grant Nos. 41705110), Beijing Municipal Natural Science Foundation (8192045) and Beijing Major Science and Technology Project (Z181100005418014). The authors are grateful to all staff and workers from the Xinglong Atmosphere Background Observation Station of the Chinese Academy of Sciences for their support during the sampling campaign.

Appendix A. Supplementary data

Supplementary data to this article can be found online at https://doi.org/10.1016/j.scitotenv.2019.135803.

References

Aiken, A., Salcedo, D., Cubison, M.J., Huffman, J., DeCarlo, P., Ulbrich, I.M., Docherty, K.S., Sueper, D., Kimmel, J., Worsnop, D.R., 2009. Mexico City aerosol analysis during MILAGRO using high resolution aerosol mass spectrometry at the urban supersite (T0)–part 1: fine particle composition and organic source apportionment. Atmos. Chem. Phys. 9, 6633–6653.

Brown, S.S., Dubé, W.P., Tham, Y.J., Zha, Q., Xue, L., Poon, S., Wang, Z., Blake, D.R., Tsui, W., Parrish, D.D., 2016. Nighttime chemistry at a high altitude site above Hong Kong. Journal of Geophysical Research: Atmospheres 121, 2457–2475.

Cañadillas, B., Westerhellweg, A., Neumann, T., 2011. Testing the performance of a ground-based wind LiDAR system: one year intercomparison at the offshore platform FINO1. Dewi Mag 38.

Canagaratna, M., Jayne, J., Jimenez, J., Allan, J., Alfarra, M., Zhang, Q., Onasch, T., Drewnick, F., Coe, H., Middlebrook, A., 2007. Chemical and microphysical characterization of ambient aerosols with the aerodyne aerosol mass spectrometer. Mass Spectrom. Rev. 26, 185–222.

Che, H., Zhang, X., Li, Y., Zhou, Z., Qu, J.J., Hao, X., 2009. Haze trends over the capital cities of 31 provinces in China, 1981–2005. Theor. Appl. Climatol. 97, 235–242.

Chen, C., Cageao, R., Lawrence, L., Stutz, J., Salawitch, R., Jourdain, L., Li, Q., Sander, S., 2011. Diurnal variation of midlatitudinal NO 3 column abundance over table mountain facility, California. Atmos. Chem. Phys. 11, 963–978.

Chen, Z., Chen, D., Cheng, N., Zhuang, Y., Kwan, M.-P., Chen, B., Zhao, B., Yang, L., Gao, B., Li, R., Xu, B., 2018. Evaluating the recent "2 + 26" regional strategy for air quality improvement during two orange air pollution alerts in Beijing: variations of $PM_{2.5}$ concentrations, source apportionment, and the relative contribution of local emission and regional transport. Atmospheric Chemistry and Physics Discussions 1–24.

DeCarlo, P.F., Kimmel, J.R., Trimborn, A., Northway, M.J., Jayne, J.T., Aiken, A.C., Gonin, M., Fuhrer, K., Horvath, T., Docherty, K.S., 2006. Field-deployable, high-resolution, time-of-flight aerosol mass spectrometer. Anal. Chem. 78, 8281–8289.

Dlugi, R., Jordan, S., Lindemann, E., 1981. The heterogeneous formation of sulfate aerosols in the atmosphere. J. Aerosol Sci. 12, 185–197.

Duan, J., Huang, R.-J., Lin, C., Dai, W., Wang, M., Gu, Y., Wang, Y., Zhong, H., Zheng, Y., Ni, H., Dusek, U., Chen, Y., Li, Y., Chen, Q., Worsnop, D.R., amp, apos, Dowd, C.D., Cao, J., 2019. Distinctions in source regions and formation mechanisms of secondary aerosol in Beijing from summer to winter. Atmospheric Chemistry and Physics Discussions 1–29.

Ge, X., He, Y., Sun, Y., Xu, J., Wang, J., Shen, Y., Chen, M., 2017. Characteristics and formation mechanisms of fine particulate nitrate in typical urban areas in China. Atmosphere 8, 62.

Guo, S., et al., 2014. Elucidating severe urban haze formation in China. Proc. Natl. Acad. Sci. U. S. A. 111 (49), 17,373–17,378.

Hu, B., Wang, Y., Liu, G., 2011. Variation characteristics of ultraviolet radiation derived from measurement and reconstruction in Beijing, China. Tellus Series B-chemical & Physical Meteorology 63, 100–108.

Hu, W., Hu, M., Hu, W., Jimenez, J.L., Yuan, B., Chen, W., Wang, M., Wu, Y., Chen, C., Wang, Z., Peng, J., Zeng, L., Shao, M., 2016. Chemical composition, sources, and aging process of submicron aerosols in Beijing: contrast between summer and winter. Journal of Geophysical Research: Atmospheres 121, 1955–1977.

Hu, W., Hu, M., Hu, W.-W., Zheng, J., Chen, C., Wu, Y., Guo, S., 2017. Seasonal variations in high time-resolved chemical compositions, sources, and evolution of atmospheric submicron aerosols in the megacity Beijing. Atmos. Chem. Phys. 17, 9979–10000.

Huang, X.F., He, L.Y., Hu, M., Canagaratna, M.R., Sun, Y., Zhang, Q., Zhu, T., Xue, L., Zeng, L.W., Liu, X.G., Zhang, Y.H., Jayne, J.T., Ng, N.L., Worsnop, D.R., 2010. Highly time-resolved chemical characterization of atmospheric submicron particles during 2008 Beijing Olympic Games using an aerodyne high-resolution aerosol mass spectrometer. Atmos. Chem. Phys. 10, 8933–8945.

Huang, R.J., Zhang, Y., Bozzetti, C., Ho, K.F., Cao, J.J., Han, Y., Daellenbach, K.R., Slowik, J.G., Platt, S.M., Canonaco, F., Zotter, P., Wolf, R., Pieber, S.M., Bruns, E.A., Crippa, M., Ciarelli, G., Piazzalunga, A., Schwikowski, M., Abbaszade, G., Schnelle-Kreis, J., Zimmermann, R., An, Z., Szidat, S., Baltensperger, U., El Haddad, I., Prevot, A.S., 2014. High secondary aerosol contribution to particulate pollution during haze events in China. Nature 514, 218–222.

Huang, X., Liu, Z., Liu, J., Hu, B., Wen, T., Tang, G., Zhang, J., Wu, F., Ji, D., Wang, L., 2017. Chemical characterization and source identification of PM 2.5 at multiple sites in the Beijing–Tianjin–Hebei region, China. Atmos. Chem. Phys. 17, 12941.

Huang, R.-J., Wang, Y., Cao, J., Lin, C., Duan, J., Chen, Q., Li, Y., Gu, Y., Yan, J., Xu, W., Fröhlich, R., Canonaco, F., Bozzetti, C., Ovadnevaite, J., Ceburnis, D., Canagaratna, M.R., Jayne, J., Worsnop, D.R., El-Haddad, I., Prévôt, A.S.H., amp, apos, Dowd, C.D., 2018. Primary emissions versus secondary formation of fine particulate matter in the top polluted city, Shijiazhuang, in North China. Atmospheric Chemistry and Physics Discussions, pp. 1–38.

Jayne, J.T., Leard, D.C., Zhang, X., Davidovits, P., Smith, K.A., Kolb, C.E., Worsnop, D.R., 2000. Development of an aerosol mass spectrometer for size and composition analysis of submicron particles. Aerosol Sci. Technol. 33, 49–70.

Ji, D., Li, L., Wang, Y., Zhang, J., Cheng, M., Sun, Y., Liu, Z., Wang, L., Tang, G., Hu, B., 2014. The heaviest particulate air-pollution episodes occurred in northern China in January, 2013: insights gained from observation. Atmos. Environ. 92, 546–556.

Jimenez, J.L., 2003. Ambient aerosol sampling using the Aerodyne Aerosol Mass Spectrometer. J. Geophys. Res. 108.

Kanakidou, M., Seinfeld, J., Pandis, S., Barnes, I., Dentener, F., Facchini, M., Dingenen, R.V., Ervens, B., Nenes, A., Nielsen, C., 2005. Organic aerosol and global climate modelling: a review. Atmos. Chem. Phys. 5, 1053–1123.

Keuken, M., Roemer, M., Elshout, S.V.D., 2009. Trend analysis of urban NO_2 concentrations and the importance of direct NO_2 emissions versus ozone/NO_x equilibrium. Atmos. Environ. 43, 4780–4783.

Lee, T., Sullivan, A.P., Mack, L., Jimenez, J.L., Kreidenweis, S.M., Onasch, T.B., Worsnop, D.R., Malm, W., Wold, C.E., Hao, W.M., 2010. Chemical smoke marker emissions during flaming and smoldering phases of laboratory open burning of wildland fuels. Aerosol Sci. Technol. 44, i–v.

Li, J., Liu, Z., Gao, W., et al., 2020. Insight into the formation and evolution of secondary organic aerosol in the megacity of Beijing, China. Atmospheric Environment 220. https://doi.org/10.1016/j.atmosenv.2019.117070.

Li, H., Zhang, Q., Zhang, Q., Chen, C., Wang, L., Wei, Z., Zhou, S., Parworth, C., Zheng, B., Canonaco, F., Prévôt, A.S.H., Chen, P., Zhang, H., He, K., 2017. Wintertime aerosol chemistry and haze evolution in an extremely polluted city of North China Plain: significant contribution from coal and biomass combustions. Atmospheric Chemistry and Physics Discussions 1–31.

Li, H., Zhang, Q., Zheng, B., Chen, C., Wu, N., Guo, H., Zhang, Y., Zheng, Y., Li, X., He, K., 2018. Nitrate-driven urban haze pollution during summertime over the North China Plain. Atmos. Chem. Phys. 18, 5293–5306.

Li, H., Cheng, J., Zhang, Q., Zheng, B., Zhang, Y., Zheng, G., He, K., 2019. Rapid transition in winter aerosol composition in Beijing from 2014 to 2017: response to clean air actions. Atmos. Chem. Phys. Discuss. 2019, 1–26.

Liu, Z., Hu, B., Wang, L., Wu, F., Gao, W., Wang, Y., 2015. Seasonal and diurnal variation in particulate matter (PM_{10} and $PM_{2.5}$) at an urban site of Beijing: analyses from a 9-year study. Environ. Sci. Pollut. Res. 22, 627–642.

Liu, Z., Hu, B., Zhang, J., Yu, Y., Wang, Y., 2016. Characteristics of aerosol size distributions and chemical compositions during wintertime pollution episodes in Beijing. Atmos. Res. 168, 1–12.

Liu, Q., Jia, X., Quan, J., Li, J., Li, X., Wu, Y., Chen, D., Wang, Z., Liu, Y., 2018a. New positive feedback mechanism between boundary layer meteorology and secondary aerosol formation during severe haze events. Sci. Rep. 8, 6095.

Liu, Z., Gao, W., Yu, Y., Hu, B., Xin, J., Sun, Y., Wang, L., Wang, G., Bi, X., Zhang, G., 2018b. Characteristics of PM 2.5 mass concentrations and chemical species in urban and background areas of China: emerging results from the CARE-China network. Atmos. Chem. Phys. 18, 8849–8871.

Liu, G., Xin, J., Wang, X., Si, R., Ma, Y., Wen, T., Zhao, L., Zhao, D., Wang, Y., Gao, W., 2019a. Impact of the coal banning zone on visibility in the Beijing-Tianjin-Hebei region. Sci. Total Environ. 692, 402–410.

Liu, Z., Hu, B., Ji, D., Cheng, M., Gao, W., Shi, S., Xie, Y., Yang, S., Gao, M., Fu, H., 2019b. Characteristics of fine particle explosive growth events in Beijing, China: seasonal variation, chemical evolution pattern and formation mechanism. Sci. Total Environ. 687, 1073–1086.

Ma, Q., Wu, Y., Zhang, D., Wang, X., Xia, Y., Liu, X., Tian, P., Han, Z., Xia, X., Wang, Y., 2017. Roles of regional transport and heterogeneous reactions in the PM2. 5 increase during winter haze episodes in Beijing. Sci. Total Environ. 599, 246–253.

Middlebrook, A.M., Bahreini, R., Jimenez, J.L., Canagaratna, M.R., 2012. Evaluation of composition-dependent collection efficiencies for the aerodyne aerosol mass spectrometer using field data. Aerosol Sci. Technol. 46, 258–271.

Millet, D.B., Baasandorj, M., Hu, L., Mitroo, D., Turner, J., Williams, B.J., 2016. Nighttime chemistry and morning isoprene can drive urban ozone downwind of a major deciduous forest. Environmental Science & Technology 50, 4335–4342.

Morgan, W., Allan, J., Bower, K., Esselborn, M., Harris, B., Henzing, J., et al., 2010. Enhancement of the aerosol direct radiative effect by semi-volatile aerosol components: airborne measurements in North-Western Europe. Atmos. Chem. Phys. 10 (17), 8151–8171.

Münkel, C., Eresmaa, N., Rasanen, J., Karppinen, A., 2007. Retrieval of mixing height and dust concentration with lidar ceilometer. Bound.-Layer Meteorol. 124, 117–128.

Paatero, P., Tapper, U., 1994. Positive matrix factorization: a non-negative factor model with optimal utilization of error estimates of data values. Environmetrics 5, 111–126.

Pan, Y., Wang, Y., Sun, Y., Tian, S., Cheng, M., 2013. Size-resolved aerosol trace elements at a rural mountainous site in Northern China: importance of regional transport. Sci. Total Environ. 461, 761–771.

Paoletti, E., 2009. Ozone and urban forests in Italy. Environ. Pollut. 157, 1506–1512.

Polissar, A., Hopke, P., Paatero, P., Kaufmann, Y., Hall, D., Bodhaine, B., Dutton, E., Harris, J., 1999. The aerosol at Barrow, Alaska: long-term trends and source locations. Atmos. Environ. 33, 2441–2458.

Prabhakar, G., Parworth, C.L., Zhang, X., Kim, H., Cappa, C.D., 2017. Observational assessment of the role of nocturnal residual-layer chemistry in determining daytime surface particulate nitrate concentrations. Atmospheric Chemistry & Physics 17, 1–58.

Quan, J., Liu, Q., Li, X., Gao, Y., Jia, X., Sheng, J., Liu, Y., 2015. Effect of heterogeneous aqueous reactions on the secondary formation of inorganic aerosols during haze events. Atmos. Environ. 122, 306–312.

Seinfeld, J.H., Pandis, S.N., 2016. Atmospheric Chemistry and Physics: From Air Pollution to Climate Change. John Wiley & Sons.

Shiraiwa, M., Ueda, K., Pozzer, A., Lammel, G., Kampf, C.J., Fushimi, A., Enami, S., Arangio, A.M., Fröhlich-Nowoisky, J., Fujitani, Y., 2017. Aerosol health effects from molecular to global scales. Environmental Science & Technology 51, 13545–13567.

Sobanski, N., Tang, M., Thieser, J., Schuster, G., Pöhler, D., Fischer, H., Song, W., Sauvage, C., Williams, J., Fachinger, J., 2016. Chemical and meteorological influences on the lifetime of NO 3 at a semi-rural mountain site during PARADE. Atmos. Chem. Phys. 16, 4867–4883.

Sun, J., Zhang, Q., Canagaratna, M.R., Zhang, Y., Ng, N.L., Sun, Y., Jayne, J.T., Zhang, X., Zhang, X., Worsnop, D.R., 2010a. Highly time- and size-resolved characterization of submicron aerosol particles in Beijing using an Aerodyne Aerosol Mass Spectrometer. Atmos. Environ. 44, 131–140.

Sun, Y.L., Zhang, Q., Schwab, J.J., Demerjian, K.L., Chen, W.N., Bae, M.S., Hung, H.M., Hogrefe, O., Frank, B., Rattigan, O.V., Lin, Y.C., 2010b. Characterization of the sources and processes of organic and inorganic aerosols in New York City with a high-resolution time-of-flight aerosol mass spectrometer. Atmospheric Chemistry and Physics Discussions 10, 22669–22723.

Sun, Y., Wang, Z., Fu, P., Jiang, Q., Yang, T., Li, J., Ge, X., 2013a. The impact of relative humidity on aerosol composition and evolution processes during wintertime in Beijing, China. Atmos. Environ. 77, 927–934.

Sun, Y.L., Wang, Z.F., Fu, P.Q., Yang, T., Jiang, Q., Dong, H.B., Li, J., Jia, J.J., 2013b. Aerosol composition, sources and processes during wintertime in Beijing, China. Atmos. Chem. Phys. 13, 4577–4592.

Sun, Y., Jiang, Q., Wang, Z., Fu, P., Li, J., Yang, T., Yin, Y., 2014. Investigation of the sources and evolution processes of severe haze pollution in Beijing in January 2013. Journal of Geophysical Research: Atmospheres 119, 4380–4398.

Sun, Y., Du, W., Wang, Q., Zhang, Q., Chen, C., Chen, Y., Chen, Z., Fu, P., Wang, Z., Gao, Z., 2015a. Real-time characterization of aerosol particle composition above the urban canopy in Beijing: insights into the interactions between the atmospheric boundary layer and aerosol chemistry. Environmental science & technology 49, 11340–11347.

Sun, Y.L., Wang, Z.F., Du, W., Zhang, Q., Wang, Q.Q., Fu, P.Q., Pan, X.L., Li, J., Jayne, J., Worsnop, D.R., 2015b. Long-term real-time measurements of aerosol particle composition in Beijing, China: seasonal variations, meteorological effects, and source analysis. Atmos. Chem. Phys. 15, 10149–10165.

Sun, Y., Jiang, Q., Xu, Y., Ma, Y., Zhang, Y., Liu, X., Li, W., Wang, F., Li, J., Wang, P., Li, Z., 2016. Aerosol characterization over the North China Plain: haze life cycle and biomass burning impacts in summer. Journal of Geophysical Research: Atmospheres 121, 2508–2521.

Tan, Z., Rohrer, F., Lu, K., Ma, X., Bohn, B., Broch, S., Dong, H., Fuchs, H., Gkatzelis, G.I., Hofzumahaus, A., 2018. Wintertime photochemistry in Beijing: observations of RO x radical concentrations in the North China Plain during the BEST-ONE campaign. Atmos. Chem. Phys. 18, 12391–12411.

Tang, G., Zhang, J., Zhu, J., et al., 2016. Mixing layer height and its implications for air pollution over Beijing, China. Atmos. Chem. Phys. https://doi.org/10.5194/acp-16-2459-2016.

Tang, G., Zhu, X., Hu, B., et al., 2015. Impact of emission controls on air quality in Beijing during APEC 2014: lidar ceilometer observations. Atmos. Chem. Phys. 15, 12667–12680. https://doi.org/10.5194/acp-15-12667-2015, 2015.

Tian, S., Pan, Y., Wang, Y., 2018. Ion balance and acidity of size-segregated particles during haze episodes in urban Beijing. Atmos. Res. 201, 159–167.

Ulbrich, I., Canagaratna, M., Zhang, Q., Worsnop, D., Jimenez, J., 2009. Interpretation of organic components from Positive Matrix Factorization of aerosol mass spectrometric data. Atmos. Chem. Phys. 9, 2891–2918.

Wang, Y., Yao, L., Wang, L., et al., 2014. Mechanism for the formation of the January 2013 heavy haze pollution episode over central and eastern China. Sci. China. Earth Sci 57 (1), 14–25.

Please cite this article as: J. Li, Z. Liu, L. Cao, et al., Highly time-resolved chemical characterization and implications of regional transport for submicron ..., Science of the Total Environment, https://doi.org/10.1016/j.scitotenv.2019.135803

Wang, Y., Zhang, X., Draxler, R.R., 2009. TrajStat: GIS-based software that uses various trajectory statistical analysis methods to identify potential sources from long-term air pollution measurement data. Environ. Model. Softw. 24, 938–939.
Wang, X., Wang, W., Yang, L., Gao, X., Nie, W., Yu, Y., Xu, P., Zhou, Y., Wang, Z., 2012. The secondary formation of inorganic aerosols in the droplet mode through heterogeneous aqueous reactions under haze conditions. Atmos. Environ. 63, 68–76.
Wang, Y., Hu, B., Tang, G., Ji, D., Zhang, H., Bai, J., Wang, X., Wang, Y., 2013. Characteristics of ozone and its precursors in Northern China: a comparative study of three sites. Atmos. Res. 132, 450–459.
Xu, J., Shi, J., Zhang, Q., Ge, X., Canonaco, F., Prévôt, A.S.H., Vonwiller, M., Szidat, S., Ge, J., Ma, J., An, Y., Kang, S., Qin, D., 2016. Wintertime organic and inorganic aerosols in Lanzhou, China: sources, processes, and comparison with the results during summer. Atmos. Chem. Phys. 16, 14937–14957.
Xu, W., Han, T., Du, W., Wang, Q., Chen, C., Zhao, J., Zhang, Y., Li, J., Fu, P., Wang, Z., Worsnop, D.R., Sun, Y., 2017. Effects of aqueous-phase and photochemical processing on secondary organic aerosol formation and evolution in Beijing, China. Environ Sci Technol 51, 762–770.
Xu, Q., Wang, S., Jiang, J., Bhattarai, N., Li, X., Chang, X., Qiu, X., Zheng, M., Hua, Y., Hao, J., 2019a. Nitrate dominates the chemical composition of PM2. 5 during haze event in Beijing, China. Sci. Total Environ. 689, 1293–1303.
Xu, W., Sun, Y., Wang, Q., Zhao, J., Wang, J., Ge, X., Xie, C., Zhou, W., Du, W., Li, J., 2019b. Changes in aerosol chemistry from 2014 to 2016 in winter in Beijing: insights from high-resolution aerosol mass spectrometry. Journal of Geophysical Research: Atmospheres 124, 1132–1147.
Xue, L., Wang, T., Gao, J., Ding, A., Zhou, X., Blake, D., Wang, X., Saunders, S., Fan, S., Zuo, H., 2014. Ground-level ozone in four Chinese cities: precursors, regional transport and heterogeneous processes. Atmos. Chem. Phys. 14, 13175–13188.
Yuan, Q., Li, W., Zhou, S., Yang, L., Chi, J., Sui, X., Wang, W., 2015. Integrated evaluation of aerosols during haze-fog episodes at one regional background site in North China Plain. Atmos. Res. 156, 102–110.
Zhang, Q., Worsnop, D., Canagaratna, M., Jimenez, J.L., 2005. Hydrocarbon-like and oxygenated organic aerosols in Pittsburgh: insights into sources and processes of organic aerosols. Atmos. Chem. Phys. 5, 3289–3311.
Zhang, J., Sun, Y., Liu, Z., Ji, D., Hu, B., Liu, Q., Wang, Y., 2014a. Characterization of submicron aerosols during a month of serious pollution in Beijing, 2013. Atmos. Chem. Phys. 14, 2887–2903.
Zhang, Y., Zhang, X., Sun, J., Hu, G., Shen, X., Wang, Y., Wang, T., Wang, D., Zhao, Y., 2014b. Chemical composition and mass size distribution of PM 1 at an elevated site in central east China. Atmos. Chem. Phys. 14, 12237–12249.
Zhang, Q., Quan, J., Tie, X., Li, X., Liu, Q., Gao, Y., Zhao, D., 2015. Effects of meteorology and secondary particle formation on visibility during heavy haze events in Beijing, China. Sci. Total Environ. 502, 578–584.
Zhang, J.K., Wang, L.L., Wang, Y.H., Wang, Y.S., 2016. Submicron aerosols during the Beijing Asia–Pacific Economic Cooperation conference in 2014. Atmos. Environ. 124, 224–231.
Zhao, P., Zhang, X., Xu, X., Zhao, X., 2011. Long-term visibility trends and characteristics in the region of Beijing, Tianjin, and Hebei, China. Atmos. Res. 101, 711–718.
Zhao, J., Du, W., Zhang, Y., Wang, Q., Chen, C., Xu, W., Han, T., Wang, Y., Fu, P., Wang, Z., Li, Z., Sun, Y., 2017. Insights into aerosol chemistry during the 2015 China Victory Day parade: results from simultaneous measurements at ground level and 260 m in Beijing. Atmos. Chem. Phys. 17, 3215–3232.
Zhao, D., Xin, J., Gong, C., Quan, J., Liu, G., Zhao, W., Wang, Y., Liu, Z., Song, T., 2019. The formation mechanism of air pollution episodes in Beijing city: insights into the measured feedback between aerosol radiative forcing and the atmospheric boundary layer stability. Sci. Total Environ. 692, 371–381.
Zhou, M., Zhang, Y., Han, Y., Wu, J., Du, X., Xu, H., Feng, Y., Han, S., 2018. Spatial and temporal characteristics of PM2. 5 acidity during autumn in marine and coastal area of Bohai Sea, China, based on two-site contrast. Atmos. Res. 202, 196–204.
Zhu, J., Che, H., Xia, X., Chen, H., Goloub, P., Zhang, W., 2014. Column-integrated aerosol optical and physical properties at a regional background atmosphere in North China Plain. Atmos. Environ. 84, 54–64.
Zhu, X., Tang, G., Hu, B., Wang, L., Xin, J., Zhang, J., Liu, Z., Münkel, C., Wang, Y., 2016. Regional pollution and its formation mechanism over North China Plain: a case study with ceilometer observations and model simulations. Journal of Geophysical Research: Atmospheres 121.

Please cite this article as: J. Li, Z. Liu, L. Cao, et al., Highly time-resolved chemical characterization and implications of regional transport for submicron ..., Science of the Total Environment, https://doi.org/10.1016/j.scitotenv.2019.135803